

LOCATION PROBLEMS OF RADIATION TYPE

D.S. Anikonov, S.G. Kazantsev

Abstract In this article we sum up the recent investigations of Anikonov D.S., Nazarov V.G. and Prokhorov I.V. in the few-projection tomography, when only a small number of projections can be recorded. In this case the possibility of full image reconstruction becomes ambiguously determined. However, it is possible to solve some other problems such as the determination of boundaries of inclusions inside an unknown medium. In the observed papers new integro-differential operators for processing the available information are proposed. These articles contain theoretical justifications of the algorithms and results of the numerical experiments. The methods proposed by Anikonov D.S., Nazarov V.G. and Prokhorov I.V. are compared with the method of D. Marr, E. Hildreth.

Key words: radiation, transport equation, inverse problems, location, image processing.

AMS Mathematics Subject Classification: 15A29, 47A52, 42C40.

1 Introduction

This paper is a review of the recent publications of Anikonov D.S., Prokhorov I.V. and Nazarov V.G. [1]–[8] dedicated to the few-projection tomography problem, in which single-beam probing or two-beam probing of an unknown medium are considered. Generally speaking computing tomography methods are widely used in biomedicine and industry. However, there are situations in the tomography, when the conditions of data recording are not perfect and it is possible to produce measurements only for few projections. Reconstruction from few projections (views) is an important problem in medical imaging and applied mathematics. Such problem arises, for example, in experiments with plasma or in a case of customs inspections of a luggage at airports. In this case the possibility of full image reconstruction becomes ambiguously determined. Therefore some other problems have been considered such as the determination of shadow boundaries of inclusions inside of an unknown medium.

In the observed articles the theoretical study and corresponding numerical experiments are given. The proposed algorithms allow to calculate the values of special integral-differential indicators for processing the available information and its subsequent visualization. The orthogonal projections (shadows) of the unknown inclusions are determined on the plane of the measurements. It is investigated the case when the direct visualization does not provide information about the structure of the medium, but after a signal processing the structure becomes clear.

Another feature of the observed methods is the consideration of scattering, unlike of many other publications in which scattering is considered only as a noise.

This article is aimed to creating tomographic algorithms of locations and can serve as the basis for new ways of orientation in arbitrary absorbing and scattering media. In

particular, these methods can be used for the detection of latent radiation sources even in the case when its radiation does not exceed background of environment radiation.

2 Mathematical model of the radiation signal

Let us consider the radiative transport equation as mathematical model of the radiation process

$$\begin{aligned} \boldsymbol{\omega} \cdot \nabla f(\mathbf{r}, \boldsymbol{\omega}) + \mu(\mathbf{r})f(\mathbf{r}, \boldsymbol{\omega}) \\ = \mu_s(\mathbf{r}) \int_{\Omega} k(\mathbf{r}, \boldsymbol{\omega} \cdot \boldsymbol{\omega}')f(\mathbf{r}, \boldsymbol{\omega}')d\boldsymbol{\omega}' + J(\mathbf{r}, \boldsymbol{\omega}), \quad (\mathbf{r}, \boldsymbol{\omega}) \in G \times \Omega, \end{aligned} \quad (1)$$

with the boundary condition

$$f(\mathbf{r} - d(\mathbf{r}, -\boldsymbol{\omega})\boldsymbol{\omega}, \boldsymbol{\omega}) = h(\mathbf{r} - d(\mathbf{r}, -\boldsymbol{\omega})\boldsymbol{\omega}, \boldsymbol{\omega}), \quad (\mathbf{r}, \boldsymbol{\omega}) \in G \times \Omega. \quad (2)$$

Here G is a convex, bounded domain in \mathbb{R}^3 with smooth boundary ∂G of class C^2 , $\Omega = \{\boldsymbol{\omega} : \boldsymbol{\omega} \in \mathbb{R}^3, |\boldsymbol{\omega}| = 1\}$ is the unit sphere and $f(\mathbf{r}, \boldsymbol{\omega})$ describes the density of particles (photons) which travel in G through the point \mathbf{r} in the direction $\boldsymbol{\omega}$. In the classical forward problem the radiation characteristics of the medium (μ – the total cross section, μ_s – the scattering cross section, k – the scattering function or the dispersion index and J – the density of internal sources of radiation) are assumed to be known. Integral term in the right-hand side of the transport equation is called the collision integral. Without loss of generality, the dispersion index $k(\mathbf{r}, \boldsymbol{\omega} \cdot \boldsymbol{\omega}')$ may be taken as the normalized function

$$\int_{\Omega} k(\mathbf{r}, \boldsymbol{\omega} \cdot \boldsymbol{\omega}')d\boldsymbol{\omega}' = 1.$$

We denote by $d(\mathbf{r}, \boldsymbol{\omega})$ the length of an intersection of the ray $L(\mathbf{r}, \boldsymbol{\omega}) = \{\mathbf{r} + t\boldsymbol{\omega}, t \geq 0\}$ and the set \overline{G} , $(\mathbf{r}, \boldsymbol{\omega}) \in \overline{G} \times \Omega$, then the points $\mathbf{r} - d(\mathbf{r}, -\boldsymbol{\omega})\boldsymbol{\omega}$ and $\mathbf{r} + d(\mathbf{r}, \boldsymbol{\omega})\boldsymbol{\omega}$ belong to ∂G . Thus function h in (2) is the density of the incident flux at the boundary of G and the problem under consideration (1)–(2) is a classical forward problem in which the function f is sought for. This problem is well studied by many authors under rather general assumptions. Note also that the solution of the equation (1) is understood in a some generalized sense. Nonnegative and bounded function

$$h_1(\mathbf{r}, \boldsymbol{\omega}) = h(\mathbf{r} - d(\mathbf{r}, -\boldsymbol{\omega})\boldsymbol{\omega}, \boldsymbol{\omega})$$

assumed to be continuous together with their first partial derivatives with respect to $(\mathbf{r}, \boldsymbol{\omega}) \in G \times \Omega$.

In order to describe the medium consisted from various substances we consider the system of disjoint domains G_i , $i = 1, \dots, p$, such that $G_i \subset G$, and denote by $G_0 = \bigcup_{i=1}^p G_i$ the union of all G_i , we also assume that $\overline{G_0} = \overline{G}$.

The domain G_i can be interpreted as the part of the inhomogeneous medium G which is filled with substance i . Clearly, that surface ∂G_0 is the union of all ∂G_i , $\partial G_0 = \bigcup_{i=1}^p \partial G_i$. We assume that for all points $\mathbf{r} \in G_0$ and all directions $\boldsymbol{\omega} \in \Omega$ the

ray $L_{\mathbf{r}, -\boldsymbol{\omega}} = \{\mathbf{r} - t\boldsymbol{\omega}, t \geq 0\}$ intersects the boundary ∂G_0 of the set G_0 in a finite number of points $\mathbf{y}_j = \mathbf{r} - t_j(\mathbf{r}, \boldsymbol{\omega})\boldsymbol{\omega}$, $j = 1, \dots, l(\mathbf{r}, -\boldsymbol{\omega})$, $0 < t_1 < \dots < t_l$. If the point \mathbf{y}_j belongs to the surface ∂G_i , $i = 1, \dots, p$, then $\mathbf{n}(\mathbf{y}_j)$ denote the inner unit normal to the surface ∂G_i , $i = 1, \dots, p$.

Let the functions μ , μ_s , k , J together with all derivatives of the first order are uniformly continuous for $(\mathbf{r}, \boldsymbol{\omega}, \boldsymbol{\omega}') \in G_i \times \Omega \times \Omega$, $i = 1, \dots, p$. On the boundaries ∂G_i , $i = 1, \dots, p$ the coefficients of the equation (1) may have non-zero discontinuities of the first type with respect the space variable \mathbf{r} . In theoretical studies we assume that the boundaries ∂G_i of domains G_i , $i = 1, \dots, p$ are piecewise smooth $2d$ surfaces of class C^2 . In general, a surface ∂G_i is considered as the Lipschitz continuous, i.e in local coordinates a small neighborhood of the boundary can be represented as a graph of function with the Lipschitz' condition.

We shall call a point $\mathbf{z} \in \partial G_0$ a contact point, if it belongs only two boundary surfaces ∂G_i , $i = 1, \dots, p$, and in some neighborhood of \mathbf{z} the surface ∂G_0 is smooth of the class C^2 . It is assumed that a set of contact points is dense in $\partial G_0 \setminus \partial G$.

The values of jumps for arbitrary function $F(\mathbf{r}, \boldsymbol{\omega})$, $\mathbf{r} = \mathbf{y}_j + t_j(\mathbf{r})\boldsymbol{\omega}$ we shall denote by $[F(\mathbf{r}, \boldsymbol{\omega})]$:

$$[F(\mathbf{r}, \boldsymbol{\omega})] = \lim_{t \rightarrow t_j+0} F(\mathbf{r} + t\boldsymbol{\omega}, \boldsymbol{\omega}) - \lim_{t \rightarrow t_j-0} F(\mathbf{r} + t\boldsymbol{\omega}, \boldsymbol{\omega}).$$

In the Fig. 1 we explain the pointed notations. Basic mathematical relation in the

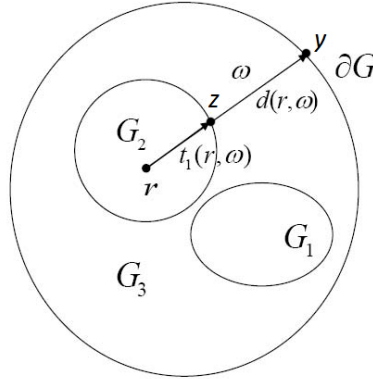


Figure 1: Domain (medium) G with two inclusions G_1 and G_2 , G_0 is the union of domains G_1 , G_2 , G_3 , $\mathbf{z} \in \partial G_0$ is a contact point, $\mathbf{y} \in \partial G$ and $\mathbf{y} = \mathbf{r} - d(\mathbf{r}, -\boldsymbol{\omega})\boldsymbol{\omega}$ are boundary points.

reviewed articles is the asymptotic formula for the gradient of the function $f(\mathbf{r}, \boldsymbol{\omega})$ with respect the space variable \mathbf{r} . The asymptotic formula for the gradient has the form

$$\begin{aligned} \nabla_{\mathbf{r}} f(\mathbf{r}, \boldsymbol{\omega}) = \\ - \sum_{j=0}^{l(\mathbf{r}, -\boldsymbol{\omega})} \exp \left(- \int_0^{t_j(\mathbf{r}, -\boldsymbol{\omega})} \mu(\mathbf{r} - t\boldsymbol{\omega}) dt \right) [\boldsymbol{\omega} \cdot \nabla_{\mathbf{r}} f(\mathbf{y}_j, \boldsymbol{\omega})] \frac{\mathbf{n}(\mathbf{y}_j)}{\mathbf{n}(\mathbf{y}_j) \cdot \boldsymbol{\omega}} + O(1), \quad (3) \end{aligned}$$

where the residual $O(1)$ is a bounded vector-function.

For the proof of this formula we refer to [9]. An obvious consequence of this formula is the fact that the gradient of function f is unbounded, if and only if $\mathbf{n}(\mathbf{y}_j) \cdot \boldsymbol{\omega} = 0$, which means that vector $\boldsymbol{\omega}$ is parallel to the tangent plane to the surface ∂G_0 at the point \mathbf{y}_j . Namely, this property is used as the basis of algorithms to solve few-projection tomography problems.

3 Setting the one projection tomography problem

Let domain G contains three subdomains G_1, G_2, G_3 with piecewise smooth boundaries of class C^2 . Define $G_4 = G \setminus (\overline{G_1} \cup \overline{G_2} \cup \overline{G_3})$ and suppose that the horizontal plane $P = (\{r_1, r_2, r_3\} : r_3 = 0\})$ crosses through the region G , but has not intersections with domains G_1, G_2, G_3 . For definiteness, we assume that the plane P is located above domains G_1, G_2, G_3 .

We denote by D the cross-section of the domain G by the the plane P and let D_1, D_2, D_3 are the vertical projections on the plane P and

$$D_4 = D \setminus (\overline{D_1} \cup \overline{D_2} \cup \overline{D_3}), \quad D_0 = D_1 \cup D_2 \cup D_3 \cup D_4.$$

Note that this assumptions don't exclude more simple cases of internal inclusions that will be used further in some numerical experiments.

Let us consider an arbitrary point $\mathbf{r} \in D_j, j = 1, 2, 3$. We denote by $\nabla_{\mathbf{r}}^* f(\mathbf{r}, \boldsymbol{\omega}_0)$ the gradient of the trace of function $f(\mathbf{r}, \boldsymbol{\omega})$ on the set D , and represent the necessary consequence of the formula (3)

$$\begin{aligned} \nabla_{\mathbf{r}}^* f(\mathbf{r}, \boldsymbol{\omega}_0) = \\ - \sum_{i=1}^{l(\mathbf{r}, -\boldsymbol{\omega}_0)} \exp \left(- \int_0^{t_j(\mathbf{r}, -\boldsymbol{\omega}_0)} \mu(\mathbf{r} - t\boldsymbol{\omega}_0) dt \right) [\boldsymbol{\omega}_0 \cdot \nabla_{\mathbf{r}} f(\mathbf{y}_j, \boldsymbol{\omega}_0)] \frac{\mathbf{n}^*(\mathbf{y}_j)}{\mathbf{n}(\mathbf{y}_j) \cdot \boldsymbol{\omega}_0} + O^*(1), \end{aligned} \quad (4)$$

where $\mathbf{n}^*(\mathbf{y}_j)$ is the orthogonal projection of the vector $\mathbf{n}(\mathbf{y}_j)$ to the plane P , $O^*(1)$ is the vector-function bounded on each subdomain D' such that $\overline{D'} \subset D$. We assume that $\overline{D'} \supset \overline{D_1} \cup \overline{D_2} \cup \overline{D_3}$.

Let us explain how to derive the equality (4) from the equation (3). First, we note that the intake of the set D' is caused with the possibility of unbounded quantities $\nabla_{\mathbf{r}}^* f(\mathbf{r}, \boldsymbol{\omega}_0)$ near the boundary of D , which can serve a hindrance for the selection of the desired lines. Secondly, instead of the complete gradient it is necessary to use only the first two its components, because the data of the problem are given on the plane P .

Note that the third component which does not used in the formula (4) is bounded. The set D' can be interpreted as an antenna wherein collimated radiation detectors are installed.

This section focuses on the formulation and study of the following one-projection tomography problem.

One-beam tomography problem. *Find (fully or partially) the boundaries $\partial D_1, \partial D_2, \partial D_3$ of domains D_1, D_2, D_3 , from the given function $f(\mathbf{r}, \boldsymbol{\omega}_0)$ for $\mathbf{r} \in D'$ and $\boldsymbol{\omega}_0 = (0, 0, 1)$.*

There are a large number of edge detection operators in the theory of image processing each of them is sensitive to certain types of edges. The method proposed in [5, 6] and solves this problem based on the equality (4). First of all, we note that the left-hand side of (4) is the gradient that is obtained from the known function. The right hand side can be unbounded, unless $\mathbf{y}_j \cdot \boldsymbol{\omega}_0 \rightarrow 0$. It is not difficult to understand that for $\mathbf{r} \in D_i$, $i = 1, 2, 3$, the last property holds only when $\rho(\mathbf{r}, \partial D_i) \rightarrow 0$. Therefore, the module of the left side of (4) may indicate the location of unknown points of ∂D_i , $i = 1, 2, 3$.

We point out and discuss five reconstruction methods.

1. Visualization of recording data $f(\mathbf{r}, \boldsymbol{\omega}_0)$ for $\mathbf{r} \in D'$ is called here the direct visibility (for example, such as a photo).
2. Visualization of processed data $|\nabla_{\mathbf{r}}^* f(\mathbf{r}, \boldsymbol{\omega}_0)|$ for $\mathbf{r} \in D'$ (direct gradient method).
3. Calculation the first integral-differential indicator

$$Ind_1(\mathbf{r}) = \int_{D'} \frac{|\nabla_{\boldsymbol{\xi}}^* f(\boldsymbol{\xi}, \boldsymbol{\omega}_0)|}{|\mathbf{r} - \boldsymbol{\xi}|^{1+\alpha}} d\boldsymbol{\xi}, \quad 0 < \alpha < 1 \quad (5)$$

and subsequent visualization.

4. Calculation the following second integral-differential indicator $Ind_2(\mathbf{r})$ and its visualization. The averaging of values $|\nabla_{\mathbf{r}}^* f(\mathbf{r}, \boldsymbol{\omega}_0)|$ carried out as follows. Let function $\chi(\boldsymbol{\xi})$ is set by the formula

$$\chi(\boldsymbol{\xi}) = \begin{cases} c_1(1 - |\boldsymbol{\xi}|^2)^2, & |\boldsymbol{\xi}| \leq 1, \boldsymbol{\xi} \in \mathbb{R}^2, \\ 0, & |\boldsymbol{\xi}| \geq 1, \boldsymbol{\xi} \in \mathbb{R}^2 \end{cases}$$

and $\int_{\mathbb{R}^2} \chi(\boldsymbol{\xi}) d\boldsymbol{\xi} = 1$.

Define $\chi_\varepsilon(\boldsymbol{\xi}) = \frac{c_1}{\varepsilon^2} \chi(\frac{\boldsymbol{\xi}}{\varepsilon})$, then

$$Ind_2(\mathbf{r}) = \int_{D'} \chi_\varepsilon(\mathbf{r} - \boldsymbol{\xi}) |\nabla_{\boldsymbol{\xi}}^* f(\boldsymbol{\xi}, \boldsymbol{\omega}_0)| d\boldsymbol{\xi}. \quad (6)$$

5. Calculation the Marr-Hildreth's indicator ([10])

$$Ind_3(\mathbf{r}) = \Delta(G * f)(\mathbf{r}) = \int_{D'} \Delta G(\boldsymbol{\xi} - \mathbf{r}) f(\boldsymbol{\xi}, \boldsymbol{\omega}_0) d\boldsymbol{\xi}, \quad (7)$$

which is the Laplacian operator of convolution signal with gaussian

$$G(\mathbf{r}) = \frac{\pi\sigma^2}{2} e^{-\frac{r^2}{2\sigma^2}}, \quad \Delta G(\mathbf{r}) = -\pi \left(1 - \frac{r^2}{2\sigma^2}\right) e^{-\frac{r^2}{2\sigma^2}}, \quad r = |\mathbf{r}|.$$

Remark, that the boundary points in the 2D image (photo) can be detected by searching for the zero values of the convolution (7) and these points correspond to the contact boundaries, see [10].

The theoretical studies have shown that the values of $|\nabla_{\mathbf{r}}^* f(\mathbf{r}, \boldsymbol{\omega}_0)|$, $Ind_1(\mathbf{r})$ and $Ind_2(\mathbf{r})$ are unbounded only near the sought lines. That is why in the numerical simulations, the set of points where these values are abnormally large are taken as the approximate solution of the one-beam tomography problem.

3.1 Algorithms testing and comparison of indicators

Firstly, in the following numerical experiment we demonstrate the algorithm based on the use of the indicator $Ind_1(\mathbf{r})$ with different values of parameter α .

In numerical calculations, for convenience, $2d$ domain D is a circle $B(\mathbf{0}, \sigma)$, and an antenna D' is the square $D' = \{\mathbf{r} = (r_1, r_2, r_3) : r_3 = 0, -0.5\sigma < r_1 < 0.5\sigma, -0.5\sigma < r_2 < 0.5\sigma\}$.

In computational experiments on finding the solution of equation (1) on the set $D' \times \boldsymbol{\omega}$ the weight versions of the Monte-Carlo methods were realized. The number of scattering events taken into account at the same time was taken as 10, and the number of paths as 100000. When the function $f(\mathbf{r}, \boldsymbol{\omega})$ have been finding in the grid nodes then the values of the indicator $Ind_1(\mathbf{r})$ are calculated for different parameters $\alpha = 0.51, 0.75, 0, 99$.

Demonstrate the work of the algorithm by the following numerical experiment intended to simulate a passive radiography search of inclusions within near-bottom zone. Let G be a ball of radius $\sigma = 80$ cm. and centered in the origin, comprising of aluminium subdomains G_1, G_2 . The sought inclusions G_1 and G_2 represent as two disjoint balls of radii 0.1σ and 0.2σ , i.e. $G_i = \{\mathbf{r} : |\mathbf{r} - \mathbf{a}_i| < 0.1i\sigma\}$, $i = 1, 2$ where $\mathbf{a}_1 = (0, 0.2\sigma, 0.5\sigma)$, $\mathbf{a}_2 = (0, -0.2\sigma, -0.5\sigma)$. The remaining two domains are defined by the relations: $G_3 = \{\mathbf{r} : r_3 < -0.1\sigma\}$, $G_4 = \{\mathbf{r} : r_3 > -0.1\sigma\}$ (see Fig. 2).

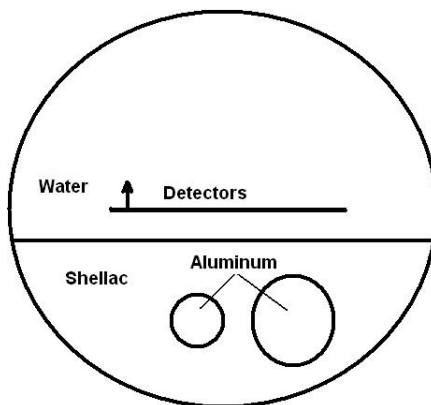


Figure 2: Layout of experiment.

In what follows G_1 and G_2 are interpreted as inclusions consisting of aluminium, the bottom part $G_3 \setminus \overline{G_1 \cup G_2}$ consists of shellac and G_4 part is filled with water (see Fig.2).

On the boundary of the domain G we set ingoing radiation $h(\mathbf{x}, \boldsymbol{\omega}) = 1$, which in our case may be interpreted as radiation background. The passive sounding of the ocean is assumed to be held at the energy 100 keV. The proper data for the coefficients of attenuation and scattering on this energy for aluminium, water and shellac were borrowed from tables [11]. The sets D_i , $i = 1, 2$ (the orthogonal projections of the sets G_i onto the plane $r_3 = 0$) belong to the square D' . The square was covered by a uniform grid holding $N_r \times N_r$ nodes at which a numerical solution of the equation (1) was found for $\boldsymbol{\omega}_0 = (0, 0, 1)$, $J(\mathbf{r}, \boldsymbol{\omega}) = 0$ within G . As far as the function $f(\mathbf{x}, \boldsymbol{\omega}_0)$ was found at the grid nodes we calculated the function $Ind_1(\mathbf{x})$ defined by formula (5). Integration

at (5) was carried out over the square D' for $\alpha = 0.51$, $\alpha = 0.75$, $\alpha = 0.99$. Number N_r was equal to 301. Results of computations for functions $f(\mathbf{x}, \boldsymbol{\omega}_0)$ and $Ind_1(\mathbf{x})$ are presented as shaded pictures on the Figs. 3 and 4. It is shown on the Fig. 3(a) that

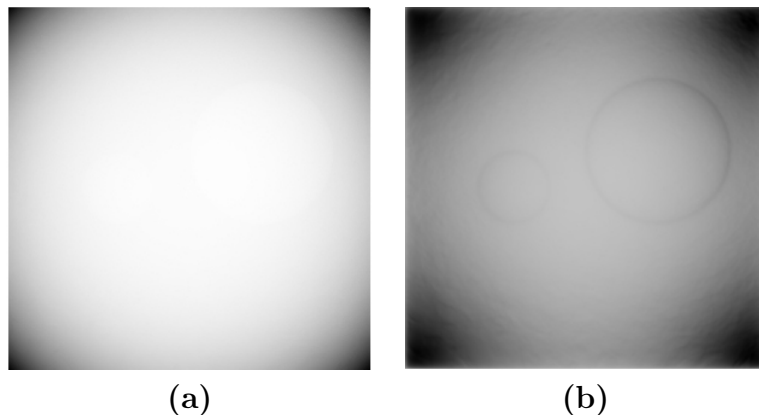


Figure 3: Results of the numerical experiment: (a) – the direct visibility or function $f(\mathbf{r}, \boldsymbol{\omega}_0)$; (b) – indicator $Ind_1(\mathbf{r})$, $\alpha = 0,51$.

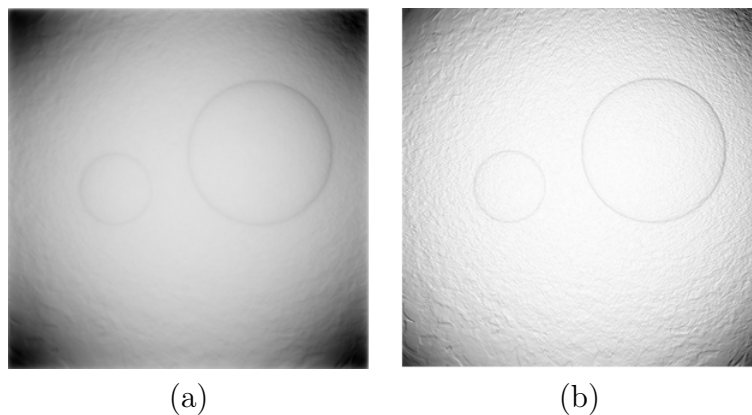


Figure 4: Results of the numerical experiment: (a)– indicator $Ind_1(\mathbf{r})$ values for $\alpha = 0,75$; (b)– indicator $Ind_1(\mathbf{r})$, $\alpha = 0,99$.

the direct visibility does not represent an information about inclusions. At the same time the shown results of the calculation helps to see the lines which are sought for. Thus, the algorithm seems to be acceptable for solving the problem considered in this article.

In the Figs.3, 4 the various heterogeneity indicators are shown. The quality of the reconstruction by using integro-differential indicator Ind_1 grows due to increasing the parameter α . In all numerical experiments the direct visualization does not allow to see the location of the desired line and as well as the direct gradient method.

Secondly in this section we demonstrate the results of numerical experiments provided by using integro-differential indicator Ind_2 . Let us illustrate how the algorithm works by simulations, which we can interpret as the problem of probing the inclusions

near the bottom of some body of water with the natural radiation of the ambient medium. In our simulations the region G is the ball of the radius $R = 10$ cm centered at the origin. The planes Q and P are given by the equations $r_3 = -0.1R$ and $r_3 = 0$, respectively. The subregion $G_1 = \{\mathbf{r} \in G : r_3 > -0.1R\}$ is filled by water. The inclusions G_3 , G_4 , and G_5 are balls of radii $0.0375R$, $0.075R$, and $0.0225R$ centered at $(0.1R, 0.1R, -0.5R)$, $(-0.1R, 0.1R, -0.5R)$, and $(0.1R, -0.1R, -0.5R)$, respectively. The subregions G_3 , G_4 , and G_5 are filled with teflon. The subregion G_2 , defined as

$$G_2 = \{\mathbf{r} \in G : r_3 < -0.1R\} \setminus (\overline{G_3} \cup \overline{G_4} \cup \overline{G_5}),$$

is filled with silt. We denote the orthogonal projections of G_3 , G_4 , and G_5 onto the plane P by D_3 , D_4 , and D_5 and these sets are sought in the problem.

While solving (1) numerically, we assume that the scattering is isotropic, that is, $k(\mathbf{r}, \boldsymbol{\omega} \cdot \boldsymbol{\omega}') = k(\mathbf{r})$. We took the values of the attenuation and scattering coefficients for the materials in the subregions G_1 , G_3 , G_4 , and G_5 from the table in [11], and for the subregion G_2 , filled with silt, we calculated them basing on the formula in [11]. All these quantities correspond to the energy $E = 100$ keV of X-ray radiation and equal respectively $\mu_1(\mathbf{r}) = 0.1707 \text{ cm}^{-1}$, $k_1(\mathbf{r}) = 0.1452 \text{ cm}^{-1}$, $\mu_2(\mathbf{r}) = 0.2082 \text{ cm}^{-1}$, $k_2(\mathbf{r}) = 0.1772 \text{ cm}^{-1}$, while $\mu_i(\mathbf{r}) = 0.3375 \text{ cm}^{-1}$ and $k_i(\mathbf{r}) = 0.2850 \text{ cm}^{-1}$ for $i = 3, 4, 5$. Thus, scattering in each of the subregions G_i for $i = 1, \dots, 5$ constituted the greater part of the attenuation coefficient. On the boundary of G we specified the incoming radiation $h_1(\mathbf{r}, \boldsymbol{\omega}) = 1$, which we interpret as a homogeneous and isotropic radiation background. We also put $J(\mathbf{r}, \boldsymbol{\omega}) = 0$ everywhere in G .

For the convenience of the simulation, we chose the square of side length $0.4R$ centered at $(0, 0, 0)$ as D' and put $\boldsymbol{\omega}_0 = (0, 0, 1)$. We cover the square by a uniform square mesh with $N \times N$ nodes at which we found the solution to problem (1), (2) for $\boldsymbol{\omega} = \boldsymbol{\omega}_0$. For convenience in the description, we also need the quantity N_ε , which stands for the number of nodes of the discretization mesh lying on the diameter of the circle $\{\mathbf{y} : (y_1 - x_1)^2 + (y_2 - x_2)^2 < \varepsilon^2\}$.

To find the solution to (1), (2) on $D' \times \boldsymbol{\omega}_0$, we use a version of the Monte Carlo method again. Since the radiation source h is distributed, we sample associated trajectories; furthermore, we calculate the free path while choosing the maximal cross-section in the material. We took 10 scattering events and 100000 trajectories. The quantity N_ε in our simulations equals 401. Once $f(\mathbf{x}, \boldsymbol{\omega}_0)$ is known at the nodes of the mesh, we calculate the function $f^*(\mathbf{x}, \boldsymbol{\omega}_0) = f(\mathbf{x}, \boldsymbol{\omega}_0) + S(\mathbf{x})$, where

$$S(\mathbf{x}) = Af(\mathbf{x}, \boldsymbol{\omega}_0)(2 - \nu(\mathbf{x})). \quad (8)$$

Here A is a nonnegative constant (the relative amplitude of white noise superimposed on $f(\mathbf{x}, \boldsymbol{\omega}_0)$) while $\nu(\mathbf{x})$ is a random function with values uniformly distributed on the interval $[0, 1]$.

Once $f(\mathbf{x}, \boldsymbol{\omega}_0)$ is known at the nodes of the mesh, we calculated by numerical integration and differentiation the functions

$$\varphi_\varepsilon^*(\mathbf{x}) = \int_{\mathbb{R}^2} \psi_\varepsilon(\mathbf{x} - \mathbf{y})f^*(\mathbf{y}, \boldsymbol{\omega}_0)d\mathbf{y}, \quad \text{Ind}_2(\mathbf{x}) = |\nabla_{\mathbf{x}}^* \varphi_\varepsilon^*(\mathbf{x})|. \quad (9)$$

Figs. 5–7 represent the results of calculations. The darker shades of grey correspond to the greater values of the function.

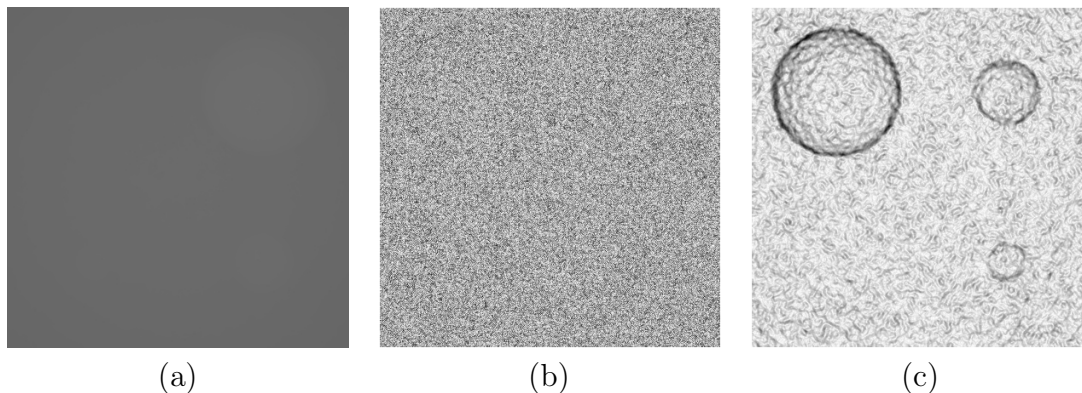


Figure 5: Distribution of functions for the noise level $A = 0.008$: (a)– direct visibility, $f^*(\mathbf{x}, \boldsymbol{\omega}_0)$; (b)– direct gradient method, $|\nabla_{\mathbf{x}}^* f^*(\mathbf{x}, \boldsymbol{\omega}_0)|$ and (c) indicator $Ind_2(x)$ for $N_\varepsilon = 9$.

In Fig.5 the useful part of the measured signal is very small, and so we cannot see the boundaries of inclusions for $f^*(\mathbf{x}, \boldsymbol{\omega}_0)$. The presence of noise prevents us from seeing the inclusions for $|\nabla_{\mathbf{x}}^* f(\mathbf{x}, \boldsymbol{\omega}_0)|$.

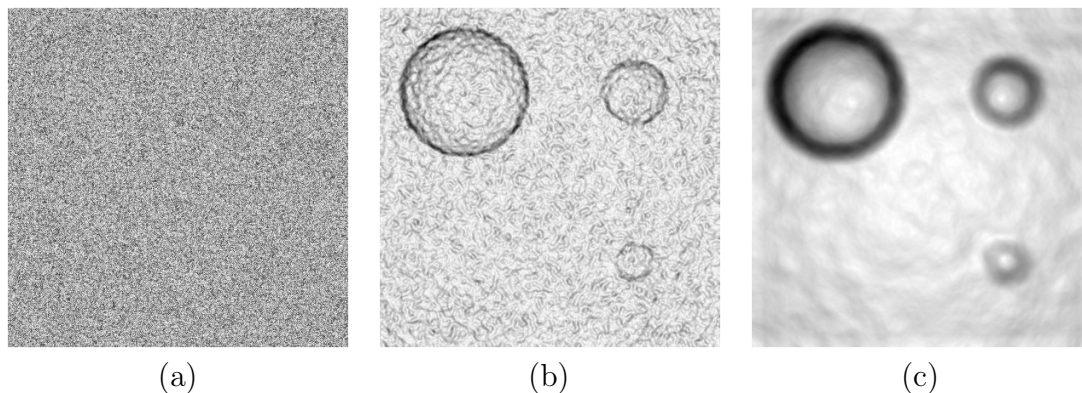


Figure 6: Analysis of images for the noise level $A = 0.008$: the values of $Ind_2(\mathbf{x})$ for (a)– $N_\varepsilon = 3$; (b)– $N_\varepsilon = 9$; and (c)– $N_\varepsilon = 33$.

It is clear from these results that the quality of images obtained by applying the indicator (6) strongly depends on the choice of the averaging parameter ε . As it increases, noise (random measurement errors) is suppressed more efficiently, but, together with that, the images of the boundaries of inhomogeneities become more blurred. Over all, the results show that the indicator $Ind_2(\mathbf{x})$ enables us to find the boundaries of inhomogeneities in the material and obtain images of sufficiently good quality in those cases when processing the images by the simple gradient method has a little effect.

In the end of this section the comparative numerical analysis of various integral-differential indicators (or image edge detection techniques) are presented. Algorithms based on the use of indicators Ind_1 , Ind_2 are compared with the Marr-Hildreth's algorithm Ind_3 . For this analysis the test used for the examination of the indicator Ind_2 is applied again. The results of the comparison are presented in the Fig. 8. As it is

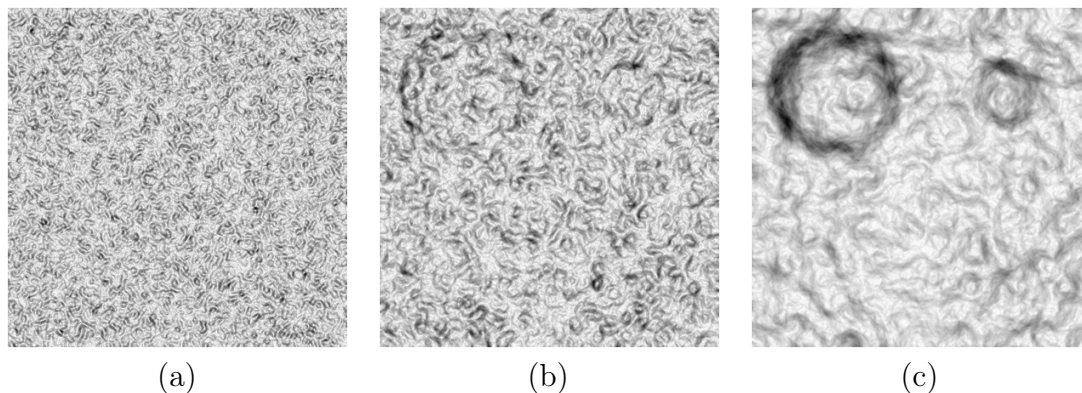


Figure 7: Analysis of images for the noise level $A = 0.064$: the values of $Ind_2(\mathbf{x})$ for (a) $N_\varepsilon = 9$; (b) $N_\varepsilon = 17$; (c) $N_\varepsilon = 33$.

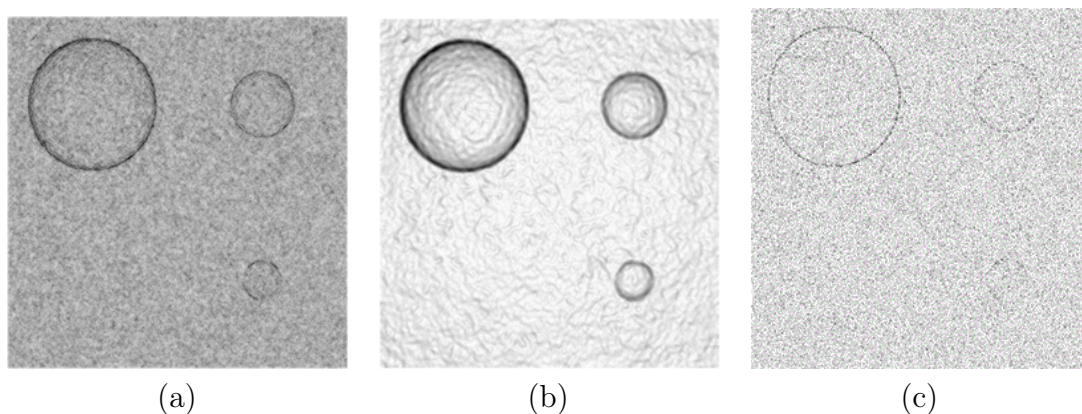


Figure 8: (a) – indicator Ind_1 ; (b)– indicator Ind_2 ; (c) – Laplacian of Gaussian(LoG) or Marr-Hildreth indicator Ind_3 .

shown the best quality of reconstruction is provided by using the indicator Ind_2 at least in the given numerical experiments.

3.2 Problem of imposing shadows of some objects to others

Here we investigate the problem of intersections of various projections of inclusions. We conclude that this intersections may improve or degrade the quality of the reconstruction according to the radiation characteristics of the medium. The reconstruction is performed by means of the direct gradient method.

Note this is the easiest, although not the best method of reconstruction. However, for the intended purpose it is sufficient, because we investigate only the influence of one inclusions to others. It is important that in this study authors essentially use the effects not only of the absorption but of scattering also. Namely, the mentioned effects take place only when the certain combinations of absorption and scattering coefficients are fulfilled.

Suppose that G is the ball of radius 1 centered at the origin, P is the plane $r_3 = 0$,

the region G_3 is the ball of radius 0.3 centered at $(0, 0, -0.5)$, G_1 is the ball of radius 0.05 centered at $(0, 0.25, -0.5)$, and G_2 is the ball of radius 0.05 centered at $(0, -0.25, -0.5)$.

We denote $G_4 = G \setminus \overline{G_3}$, $\mathbf{z}_1 = (0, 0.3, 0)$, $\mathbf{z}_2 = (0, -0.3, 0)$. Take $J = 0$ and $h = 1$. Let μ_i and $\mu_{s,i}$ be the values of the piecewise constant coefficients μ and μ_s on G_i , $i = 1, 2, 3, 4$. The sets D_i , $i = 1, 2, 3$, are the orthogonal projection of G_i onto the plane $r_3 = 0$.

Take the values

$$\mu_1 = 9, \mu_{s,1} = 1.5, \mu_2 = 9, \mu_{s,2} = 4.5,$$

$$\mu_3 = 7.5, \mu_{s,3} = 3, \mu_4 = 6.9, \mu_{s,4} = 3.6.$$

Consider the ray $L_{\mathbf{r}, -\boldsymbol{\omega}_0} = \{\mathbf{r} + t(-\boldsymbol{\omega}_0), t \geq 0\}$ for $\mathbf{r} \in D_1$, $\boldsymbol{\omega}_0 = (0, 0, 1)$. It intersects the boundary of the balls G_3 and G_1 at $\mathbf{y}_1, \mathbf{y}_2, \mathbf{y}_3$, and \mathbf{y}_4 , which we read in the succession as t increases. Consequently,

$$\mathbf{y}_1 \in \partial G_4 \cap \partial G_3, \mathbf{y}_2 \in \partial G_1 \cap \partial G_3, \mathbf{y}_3 \in \partial G_1 \cap \partial G_3, \mathbf{y}_4 \in \partial G_4 \cap \partial G_3.$$

Counting the jumps of an arbitrary function $F(\mathbf{y})$ along the ray $\mathbf{y}_j = \mathbf{r} + t_j(-\boldsymbol{\omega}_0)$ as

$$[F(\mathbf{y}_j)] = \lim_{t \rightarrow t_j+0} F(\mathbf{r} - t\boldsymbol{\omega}_0) - \lim_{t \rightarrow t_j-0} F(\mathbf{r} - t\boldsymbol{\omega}_0)$$

we obtain

$$[\mu(\mathbf{y}_1)] = 0.6, [\mu_{s,1}(\mathbf{y}_1)] = 0.6, [\mu(\mathbf{y}_2)] = 1.5, [\mu_{s,1}(\mathbf{y}_1)] = 1.5,$$

$$[\mu(\mathbf{y}_3)] = 1.5, [\mu_{s,1}(\mathbf{y}_3)] = 1.5, [\mu(\mathbf{y}_4)] = 0.6, [\mu_{s,1}(\mathbf{y}_4)] = 0.6.$$

We can see that, in this case, the overlap of the projections (shadows) of D_1 with D_3 must lead to improving the reconstruction of the required lines near \mathbf{z}_1 . Arguing similarly for D_2 and using the same notation $\mathbf{y}_1, \mathbf{y}_2, \mathbf{y}_3$, and \mathbf{y}_4 for the points of intersection of the ray $L_{\mathbf{r}, -\boldsymbol{\omega}_0}$ and the boundaries of the balls G_3 and G_2 , we obtain

$$[\mu(\mathbf{y}_1)] = 0.6, [\mu_{s,1}(\mathbf{y}_1)] = -0.6, [\mu(\mathbf{y}_2)] = 1.5, [\mu_{s,1}(\mathbf{y}_2)] = 1.5,$$

$$[\mu(\mathbf{y}_3)] = -1.5, [\mu_{s,1}(\mathbf{y}_3)] = -1.5, [\mu(\mathbf{y}_4)] = -0.6, [\mu_{s,1}(\mathbf{y}_4)] = 0.6,$$

where

$$\mathbf{y}_1 \in \partial G_4 \cap \partial G_3, \mathbf{y}_2 \in \partial G_2 \cap \partial G_3, \mathbf{y}_3 \in \partial G_2 \cap \partial G_3, \mathbf{y}_4 \in \partial G_4 \cap \partial G_3.$$

According to the arguments of [6] in this case the reconstruction of the lines near \mathbf{z}_2 must worsen. Let us demonstrate the work of the algorithm on the following numerical example. On the surface of G we define the incoming radiation $h(\mathbf{r}, \boldsymbol{\omega}) = 1$, which in our case we can interpret as background radiation. The set D' is a circle of radius 1, while, for the convenience of computations, we took as D' the square

$$D' = \{\mathbf{r} = (r_1, r_2, r_3) : r_3 = 0, 0.5 < r_1 < 0.5, 0.5 < r_2 < 0.5\}.$$

Therefore, the sets $D_i, i = 1, 2, 3$ (orthogonal projections of G_i onto the plane $r_3 = 0$) would lie in the square D' . Then D' is covered by a uniform mesh containing

$N_r \times N_r$ nodes, at which we determine numerically the solution to (1) for $\boldsymbol{\omega}_0 = (0, 0, 1)$; moreover, we put $J(\mathbf{r}, \boldsymbol{\omega}) = 0$ in G . In order to find a solution to (1) on D' we also used one of the versions of the Monte Carlo method called the adjoint walks method with choice of the maximal cross-section for modelling free runs. The number of considered acts of scattering was 10, and the number of trajectories was 100 000.

Upon finding the function $f(\mathbf{r}, \boldsymbol{\omega}_0)$ at the nodes of the mesh, we calculated the values of $|\nabla_{\mathbf{r}}^* f(\mathbf{r}, \boldsymbol{\omega}_0)|$. The calculations were restricted to the square D' . The quantity N_r in the computations is equal to 301. The figure depicts the results of the calculations of $f(\mathbf{r}, \boldsymbol{\omega}_0)$ and $|\nabla_{\mathbf{r}}^* f(\mathbf{r}, \boldsymbol{\omega}_0)|$. As we can see, a direct visualization fails to enable us to distinguish the required lines. In the part of the figure corresponding to reconstruction using our algorithm, we can distinguish the greater inclusion, as well as two smaller ones inside it. Moreover, the quality of the lower part of the image is noticeably worse than in its upper part, which fully agrees with the theoretical conclusions on the possibility of improvement or worsening of the image due to overlapping shadows depending on the parameters of the problem. In principle, the total indistinguishability of the lower part of the reconstruction would be possible, but the variant we chose better serves the purpose of our study.

In the test we used certain combinations of the absorption and scattering coefficients. Let us emphasize that, it would be impossible if we refuse to take scattering into account. Note also that we chose so great optical distance from the plane of measurements to the inclusions and sufficiently noticeable level of scattering that a direct visualization was impossible. This test turned out difficult for our algorithm neither. This is the reason for a comparatively low sharpness of our reconstruction in the right part of the figure. Together with that, the result seems quite sufficient for our goals (see Fig.9).

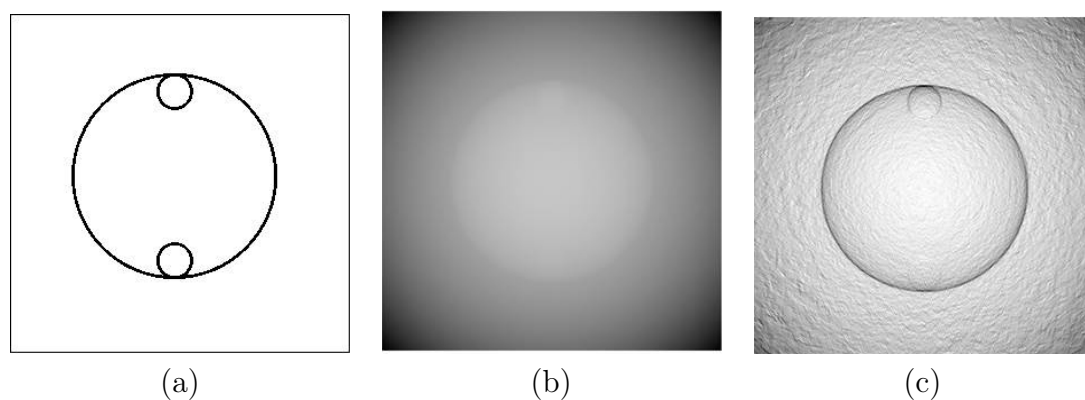


Figure 9: Results of the numerical experiment: (a)– projections of the boundaries of G_1 , G_2 and G_3 onto the plane P ; (b) – the values of $f(\mathbf{r}, \boldsymbol{\omega}_0)$ at the nodes of the mesh covering D' (direct visibility); (c) – the values of $|\nabla_{\mathbf{r}}^* f(\mathbf{r}, \boldsymbol{\omega}_0)|$ at the nodes of the mesh. It can be seen that the reconstruction of the upper inner ball is better than the reconstruction of the lower ball.

4 Two-beam tomography problem

In two-beam tomography problem two directions of the radiation will be used and thus the result will differ from the previous one. In the previous case we determined only a shadow of the object on the plane of measurements (antenna), but now it will be possible to locate the body in the space.

For simplicity, we consider the case, when the medium has only one substance G_1 . We introduce the following notation: let G_1, G_2 be bounded domains in \mathbb{R}^3 with smooth boundary of class C^2 , thus $\overline{G_1} \subset G, G_2 \subset G \setminus \overline{G_1}$ and $C(T, \boldsymbol{\omega})$ be a cylinder in \mathbb{R}^3 based on $2d$ set T with the direction (generatrix) $\boldsymbol{\omega}$, i.e. the union of points which lie on all rays $L(\boldsymbol{\tau}, \pm\boldsymbol{\omega}), \boldsymbol{\tau} \in T$.

We formulate now the two-beam tomography problem and introduce the following notation, see [7]. Let P and Q are two planes in \mathbb{R}^3 which are not crossing the G_1 , but having a non-empty intersection with G_2 . Denoted by $\boldsymbol{\omega}_P = (\omega_{P1}, \omega_{P2}, \omega_{P3}), \boldsymbol{\omega}_Q = (\omega_{Q1}, \omega_{Q2}, \omega_{Q3})$ the unit normals to the plans P and Q , correspondingly, and assume that the vectors $\boldsymbol{\omega}_P$ and $\boldsymbol{\omega}_Q$ are linearly independent. Consider also the two plane domains $\overline{P_1} \subset P \cap G_2$ and $\overline{Q_1} \subset Q \cap G_2$, so that each of cylinders $C(P_1, \boldsymbol{\omega}_P), C(Q_1, \boldsymbol{\omega}_Q)$ strictly contain domain G_1 . For convenience hereinafter we will write variable \mathbf{r} as $\mathbf{x} \equiv \mathbf{r}$ if $\mathbf{r} \in P_1$ and as $\mathbf{y} \equiv \mathbf{r}$ if $\mathbf{r} \in Q_1$. Denote by D_P and D_Q the orthogonal projection of G_1 to the plane P and Q , respectively.

Two-beam tomography problem: *The problem of two-beam tomography consists in obtaining information about domain G_1 from two known functions $f(\mathbf{x}, \boldsymbol{\omega}_P), \mathbf{x} \in P_1$ and $f(\mathbf{y}, \boldsymbol{\omega}_Q), \mathbf{y} \in Q_1$.*

More specifically, the goal is to construct and justify an algorithm for finding the intersection of the cylinders $C(D_P, \boldsymbol{\omega}_P)$ and $C(D_Q, \boldsymbol{\omega}_Q)$.

The plane domains P_1 and Q_1 can be interpreted as antennas which are oriented to investigated object and they fix a probe signal collimated in orthogonal directions to planes of the antennas. Using this information we must specify the shape of the body G_1 and its location in the space. This notations are illustrated in Fig. 10.

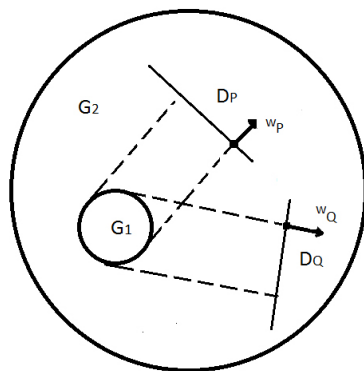


Figure 10: Two-beam tomography.

4.1 Algorithm of two-beam tomography

Here we describe the algorithm process to solve the two-beam tomography problem. Note that for this problem it was used already approved the indicator of heterogeneity $Ind_1(\mathbf{r})$.

Let $\nabla_P f(\mathbf{x}, \boldsymbol{\omega}_P)$ and $\nabla_Q f(\mathbf{y}, \boldsymbol{\omega}_Q)$ be two-dimensional gradients with respect to \mathbf{r} for traces of the function $f(\mathbf{r}, \boldsymbol{\omega})$ when $\mathbf{r} = \mathbf{x} \in P_1$, $\boldsymbol{\omega} = \boldsymbol{\omega}_P$ and when $\mathbf{r} = \mathbf{y} \in Q_1$, $\boldsymbol{\omega} = \boldsymbol{\omega}_Q$. For each of these gradients, we define the indicator of heterogeneity

$$Ind_1(\mathbf{x}) = \int_{P_1} \frac{|\nabla_P f(\boldsymbol{\xi}, \boldsymbol{\omega}_P)|}{|\mathbf{x} - \boldsymbol{\xi}|^{1+\alpha}} d\boldsymbol{\xi}, \quad Ind_1(\mathbf{y}) = \int_{Q_1} \frac{|\nabla_Q f(\boldsymbol{\xi}, \boldsymbol{\omega}_Q)|}{|\mathbf{y} - \boldsymbol{\xi}|^{1+\alpha}} d\boldsymbol{\xi}, \quad 1/2 < \alpha < 1.$$

It is clear that $\overline{D_P} \subset P_1$ and $\overline{D_Q} \subset Q_1$. Under certain restrictions, which are performed in observed papers, it was proved that $Ind_1(\mathbf{x}) \rightarrow \infty$, $Ind_1(\mathbf{y}) \rightarrow \infty$ if and only if $\mathbf{x} \in D_P$, $\mathbf{x} \rightarrow \partial D_P$, $\mathbf{y} \in D_Q$, $\mathbf{y} \rightarrow \partial D_Q$, see [5]. From this it follows the uniqueness of finding the projections (shadows) D_P and D_Q to the corresponding planes. Hence the points with anomalously large values of function $Ind_1(\mathbf{x})$ and $Ind_1(\mathbf{y})$ correspond to boundaries ∂D_P and ∂D_Q . This statement is the base of the following algorithm, which was developed and implemented in [7].

The main steps of this algorithm are the following:

- a) find D_P and D_Q using indicators of heterogeneity $Ind_1(\mathbf{x})$, $Ind_1(\mathbf{y})$;
- b) fix any point $\mathbf{x} = (x_1, x_2, x_3) \in D_P$;
- c) solve the system of two linear equations for \mathbf{y} , one of which is

$$(\mathbf{y} - \mathbf{x}) \cdot (\boldsymbol{\omega}_P \times \boldsymbol{\omega}_Q) = 0, \quad (10)$$

and the other is the equation of the plane Q , here \times is the cross product;

- d) the set of the solutions $\mathbf{y} = (y_1, y_2, y_3)$ is a straight line, but we choose those points that belong to D_Q ;
- e) for each selected point $\mathbf{y} = (y_1, y_2, y_3) \in D_Q$ and the previously fixed point $\mathbf{x} = (x_1, x_2, x_3) \in D_P$ we solve the next system with respect to values $t(\mathbf{x})$ and $t(\mathbf{y})$

$$\begin{cases} t(\mathbf{x})\omega_{P1} - t(\mathbf{y})\omega_{Q1} = y_1 - x_1 \\ t(\mathbf{x})\omega_{P2} - t(\mathbf{y})\omega_{Q2} = y_2 - x_2 \\ t(\mathbf{x})\omega_{P3} - t(\mathbf{y})\omega_{Q3} = y_3 - x_3, \end{cases}$$

the existence of a solution of this predetermined system is ensured by the item c) and d);

- f) finally, the points $\mathbf{r} = \mathbf{x} + t(\mathbf{x})\boldsymbol{\omega}_P = \mathbf{y} + t(\mathbf{y})\boldsymbol{\omega}_Q$ give the spatial localization of the domain G_1 .

The values $t(\mathbf{x})$ and $t(\mathbf{y})$ are equal to the distances from the antenna to the point of intersection of the rays $L(\mathbf{x}, -\boldsymbol{\omega}_P)$ and $L(\mathbf{y}, -\boldsymbol{\omega}_Q)$, i.e. indicate the approximate distances to the seeking object.

Note that this algorithm may be easy extended to the case of a large number of angles. However, basically, this does not change the situation and we derive only some improvement of the form and position of the domain G_1 .

4.2 Testing of the algorithm

Let G be the ball $B(\mathbf{0}, \rho)$ centered at the origin of radius ρ , and let G_1 be another ball: $G_1 = B(\mathbf{z}, \rho_1)$, where $\mathbf{z} = (z_1, z_2, z_3)$ and $0 < \rho_1 < \rho$. This simple case is chosen, on the one hand, to simplify the complex computations for $f(\mathbf{r}, \boldsymbol{\omega})$ and, on the other hand, since the shape of the unknown inclusion is not important for the algorithm to be tested.

The planes P and Q are defined by the equations $(\mathbf{x} - \mathbf{a}, \boldsymbol{\omega}_P) = 0$ and $(\mathbf{y} - \mathbf{b}, \boldsymbol{\omega}_Q) = 0$, where $\mathbf{a} = (a_1, a_2, a_3)$ and $\mathbf{b} = (b_1, b_2, b_3)$. The plane domains P_1 and Q_1 are squares centered at the points \mathbf{a} and \mathbf{b} with side lengths $\beta\rho_1$, $\beta > 2$.

The parameter values in the computations were specified as $\rho = 1$ cm, $\rho_1 = 0.1\rho$, $\mathbf{z} = (0.1\rho, -0.1\rho, -0.2\rho)$, $\boldsymbol{\omega}_P = (0, 0, 1)$, $\boldsymbol{\omega}_Q = (\sqrt{2}/2, 0, \sqrt{2}/2)$, $\mathbf{a} = (0.1\rho, -0.1\rho, 0)$, and $\mathbf{b} = (0.3\rho, -0.1\rho, 0)$. The values of $\mu_1(\mathbf{r})$ and $k(\mathbf{r}) = \int_{\Omega} k(\mathbf{r}, \boldsymbol{\omega} \cdot \boldsymbol{\omega}') d\boldsymbol{\omega}'$ in G_1 correspond to aluminum with an energy value of 100 keV, while $\mu_2(\mathbf{r})$ and $k_2(\mathbf{r})$ in G_2 correspond to water with the same energy. More specifically, $\mu_1(\mathbf{r}) = 0.4599 \text{ cm}^{-1}$, $k_1(\mathbf{r}) = 0.3575 \text{ cm}^{-1}$, $\mu_2(\mathbf{r}) = 0.1707 \text{ cm}^{-1}$, and $k_2(\mathbf{r}) = 0.1452 \text{ cm}^{-1}$. These values were taken from tables, see [11]. The value of J everywhere in G was set to zero. The function $h(\mathbf{r}, \boldsymbol{\omega})$ was everywhere equal to unity.

The measuring sensors were placed at the nodes of a uniform square 101×101 grid covering P_1 for the plane P (or Q_1 for the plane Q) with the side length $4\rho_1$.

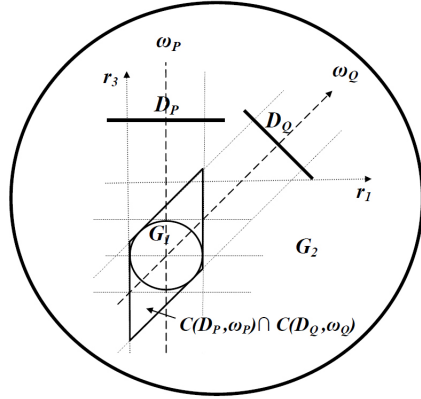


Figure 11: Part of the section of G by the plane $r_2 = -0.1\rho$ passing through the center of G_1 , and the boundary of $C(D_P, \boldsymbol{\omega}_P) \cap C(D_Q, \boldsymbol{\omega}_Q)$.

According to the above parameter values, the plane P was defined by the equation $r_3 = 0$, while the plane Q , by the equation $(\mathbf{y} - \mathbf{b}, \boldsymbol{\omega}_Q) = 0$ or, with \mathbf{r} denoted by \mathbf{y} , by the equation

$$y_1 - 0.3\rho + y_3 = 0. \quad (11)$$

Following the above described computational scheme, we first solved equation (1) with boundary condition (2) and determined the function $f(\mathbf{x}, \boldsymbol{\omega}_P)$ at grid nodes covering $P_1 \subset P$. Then the indicator $Ind_1(\mathbf{x})$ was calculated at the same nodes. The same was performed for the square $Q_1 \subset Q$. More specifically, the function $f(\mathbf{y}, \boldsymbol{\omega}_Q)$ was found

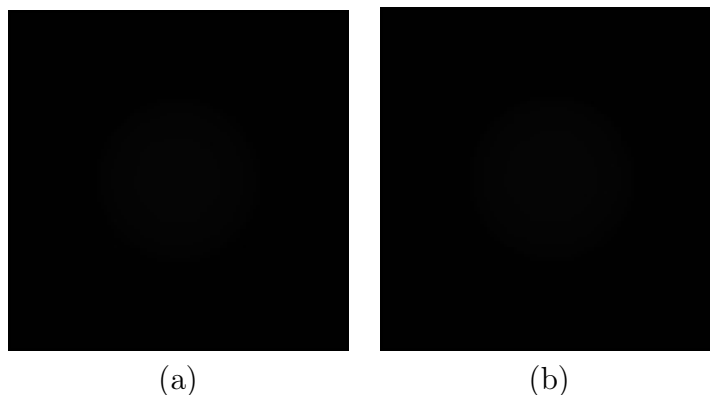


Figure 12: (a)– the values of $f(\mathbf{x}, \boldsymbol{\omega}_P)$ found at nodes of a uniform square 101×101 grid covering the square P_1 for the plane P at $\alpha = 0.9$ and (b)– the values of $f(\mathbf{y}, \boldsymbol{\omega}_Q)$ found at nodes of a uniform square 101×101 grid covering the square Q_1 for the plane Q at $\alpha = 0.9$.

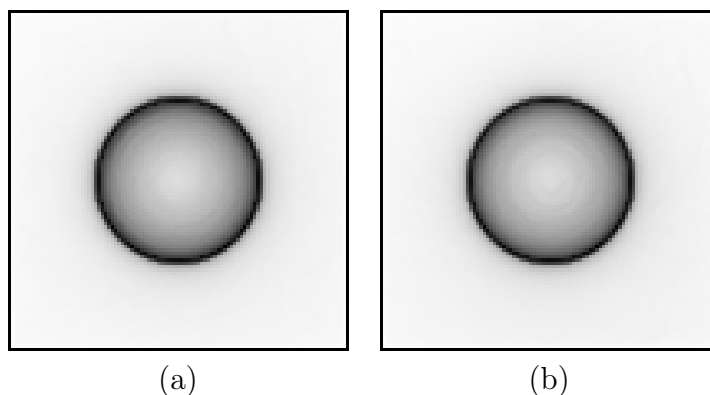


Figure 13: (a)– the values of $Ind_1(\mathbf{x})$ found at nodes of a uniform square 101×101 grid covering the square P_1 for the plane P at $\alpha = 0.9$ and (b)– $Ind_1(\mathbf{y})$ found at nodes of a uniform square 101×101 grid covering the square Q_1 for the plane Q at $\alpha = 0.9$. The test conditions (i.e., the absorption and scattering of the medium) are such that direct visualization (see Fig.12 (a),(b)) does not produce an image of the desired object, while the reconstruction with the help of the indicator yields a clear boundary of the shadow of G_1 .

and, then, the corresponding indicator $Ind_1(\mathbf{y})$ was calculated. The computations were performed at $\alpha = 0.9$. The numerical results for P and Q are presented in Figs.12 and 13, respectively. Specifically, the domains of $f(\mathbf{x}, \boldsymbol{\omega}_P)$ and $f(\mathbf{y}, \boldsymbol{\omega}_Q)$ are depicted in Figs.12(a), 12(b). and the domains of $Ind_1(\mathbf{x})$ and $Ind_1(\mathbf{y})$ are presented in Figs.13(a), 13(b). Larger function values are shown by darker shades. Thus, the points where the corresponding functions have anomalously large values are emphasized. Figs.12(a) and 12(b) look like solid squares, since $f(\mathbf{x}, \boldsymbol{\omega}_P)$ and $f(\mathbf{y}, \boldsymbol{\omega}_Q)$ vary insignificantly and the projections of G_1 cannot be seen against them without special signal processing.

Thus, we have found the sets D_P and D_Q .

Now, we fix a point $\mathbf{x} \in D_P$. Let $\mathbf{x} = (0.1\rho, -0.1\rho, 0)$. The corresponding system of

equations (10) and (11) has the form

$$(\mathbf{y} - \mathbf{x}) \cdot (\boldsymbol{\omega}_P \times \boldsymbol{\omega}_Q) = 0, \quad y_3 = 0.3\rho - y_1,$$

or

$$y_2 + 0.1\rho = 0, \quad y_3 = 0.3\rho - y_1. \quad (12)$$

It is easy to see that the solution set of system (12), which belongs to D_Q , is given by

$$y_2 = -0.1\rho, \quad y_3 = 0.3\rho - y_1, \quad 0.3\rho - \sqrt{2}\rho/20 < y_1 < 0.3\rho + \sqrt{2}\rho/20.$$

With chosen P and Q , system from the step e) has the form

$$\begin{cases} -t(\mathbf{y})\sqrt{2}/2 = y_1 - 0.1\rho \\ 0 = y_2 + 0.1\rho \\ t(\mathbf{x}) - t(\mathbf{y})\sqrt{2}/2 = y_3 \end{cases}$$

whence

$$t(\mathbf{x}) = y_3 - y_1 + 0.1\rho = 0.4\rho - 2y_1, \quad t(\mathbf{y}) = 2/\sqrt{2}(0.1\rho - y_1).$$

Thus, the set of all points from $C(D_P, \boldsymbol{\omega}_P) \cap C(D_Q, \boldsymbol{\omega}_Q)$ obtained with the help of the preliminarily chosen point $\mathbf{x} = (0.1\rho, -0.1\rho, 0) \in D_P$, i.e., the localization of G_1 , has the form $\mathbf{r} = \mathbf{x} + t(\mathbf{x})\boldsymbol{\omega}_P = (0.1\rho, -0.1\rho, 0.4\rho - 2y_1)$, where

$$0.3\rho - \sqrt{2}\rho/20 < y_1 < 0.3\rho + \sqrt{2}\rho/20. \quad (13)$$

If \mathbf{y} is specified, for example, as the point \mathbf{b} , so that $\mathbf{y} = (0.3\rho, -0.1\rho, 0)$, then we obtain $\mathbf{r} = (0.1\rho, -0.1\rho, -0.2\rho) = \mathbf{z}$, i.e., the center of the ball G_1 .

If the point $\mathbf{y} \in D_Q$ is chosen too close to the boundary of range (13), then the resulting points $\mathbf{r} = \mathbf{x} + t(\mathbf{x})\boldsymbol{\omega}_P = \mathbf{y} + t(\mathbf{y})\boldsymbol{\omega}_Q$ do not belong to G_1 , while lying inside $C(D_P, \boldsymbol{\omega}_P) \cap C(D_Q, \boldsymbol{\omega}_Q)$. Indeed, let $y_1 = 0.3\rho + \delta$, where $\rho/20 < |\delta| < \sqrt{2}\rho/20$. Then

$$|\mathbf{r} - \mathbf{z}| = |\mathbf{x} + t(\mathbf{x})\boldsymbol{\omega}_P - \mathbf{z}| = |0.4\rho - 2(0.3\rho + \delta) + 0.2\rho| = 2\delta > 0.1\delta,$$

i.e., $\mathbf{r} \notin G_1$.

The test conditions (i.e., the absorption and scattering of the medium) are such that direct visualization (see Fig.12) does not produce an image of the desired object, while the reconstruction with using the indicator (see Fig.13) yields a clear boundary of the shadow of G_1 . Fig.11 schematically shows part of the section of G by the plane $r_2 = -0.1\rho$ passing through the center of the inclusion G_1 .

In this section, the boundary of $C(D_P, \boldsymbol{\omega}_P) \cap C(D_Q, \boldsymbol{\omega}_Q)$ is the rhombus with side lengths $\sqrt{2}\rho/5$ and vertexes at the points $(0, -0.1\rho, -0.1\rho(\sqrt{2} + 3))$ (lower corner), $(0.2\rho, -0.1\rho, -0.1\rho(\sqrt{2} + 1))$ (right corner), $(0.2\rho, -0.1\rho, 0.1\rho(\sqrt{2} - 1))$ (upper corner) and $(0, -0.1\rho, 0.1\rho(\sqrt{2} - 3))$ (left corner), see Fig. 11.

In conclusion we emphasize that this review is concerned with an only certain part of signal processing theory. The main feature of the reviewed articles is an application of a transport integral differential equation as a mathematical model of a probing signal which allows us to take into account the effects of the absorption and scattering simultaneously.

Acknowledgement

The authors were supported by the Russian Foundation for Basic Research (Grant 13-01-00275).

References

- [1] Anikonov D.S., Prokhorov I.V., Nazarov V.G., Solnyshko N.V., *The method for masking of products*, Patent of Russian Federation № 2264424. Bulletin No. 32, 20.11.2005, application No. 2003124026 from 30.07.2003.
- [2] Anikonov D.S., Kovtanyuk A.E., Nazarov V.G., Prokhorov I.V., Surovenkov N.S., Yarovenko I.P., *Database of radiation characteristics of substances, interested in radiology*, Certificate of state registration of computer programs database No. 2009620348, registered in the Registry database 19.06.2009. Published in the official bulletin "Computer programs, databases, topology of microcircuitry". 2009, No. 3, pp. 334–335.
- [3] Anikonov D.S., Kovtanyuk A.E., Nazarov V.G., Prokhorov I.V., Surovenkov N.S., Yarovenko I.P., *The contrast determination of an inhomogeneous medium in X-ray tomography*, Certificate of state registration of computer programs database N 2009613135, registered in the computer program register 16.06.2009. Published in the official bulletin "Computer programs, databases, topology of microcircuitry". 2009, No. 4, pp. 479–480. It is registered in the Register of programs on 30 July 2012, bulletin No. 4.
- [4] Anikonov D.S., Nazarov V.G., *Improvement of the quality of two-dimensional images in problems of one-beam tomography*, Certificate state registration of the computer programm No. 201261870, 2012.
- [5] Anikonov D.S., Nazarov V.G., Prokhorov I.V., *Algorithm of finding a body projection within an absorbing and scattering medium*, Journal of Inverse and Ill-Posed Problems, Vol. 19, Issue 2(2011), pp. 11–19.
- [6] Anikonov D. S., Nazarov V. G. and Prokhorov I. V., *The Problem of Single-Beam Probing of an Unknown Medium*, J. Appl. Indust. Math., Vol.5, Issue 4(2011), pp. 500–505.
- [7] Anikonov D.S., Nazarov V.G., *Problem of Two-Beam Tomography*, Computational Mathematics and Mathematical Physics, Vol.52, Issue 3(2012), pp. 372–378.
- [8] Anikonov D. S., Nazarov V.G., Prokhorov I.V., *The integro-differential indicator for a problem of single-beam tomography*, Journal of Applied and Industrial Mathematics, Vol. 8, Issue 3(2014), pp. 1-8.
- [9] Anikonov D.S., Kovtanyuk A.E. and Prokhorov I.V., *Transport Equation and Tomography*, Utrecht-Boston: VSP, 2002.
- [10] D. Marr, E. Hildreth, *Theory of Edge Detection*, Proceedings of the Royal Society of London. Series B, Biological Sciences, Vol. 207, Issue 1167(1980), pp. 187-217.
- [11] Hubbell J.H., Seltzer S.M., *Tables of X-ray mass attenuation coefficients and mass energy-absorption coefficients 1Kev to 20Mev for elements Z = 1 to 92 and 48 additional substances of dosimetric interest*, NISTIR 5632. 1995.

D.S. Anikonov

Sobolev Institute of Mathematics, Siberian Branch of Russian Academy of Sciences,
prosp. Acad. Koptyug, 4, Novosibirsk 630090, Russia,

Email: anik@math.nsc.ru.

S. G. Kazantsev,
Sobolev Institute of Mathematics, Siberian Branch of Russian Academy of Sciences,
prosp. Acad. Koptug, 4, Novosibirsk 630090, Russia,
Email: kazan@math.nsc.ru.

Received 19.02.2015, Accepted 01.03.2015